Advanced Robotics Research

ADVANCED ROBOTICS RESEARCH Open Access

RESEARCH ARTICLE OPEN ACCESS

A Soft Robotic Device for Targeted Massage Therapy of Residual Limbs

Maria Grazia Polizzotto[1] | Alessio Capecchi[1] | Maartje Van der Lingen[1] | Emanuele Gruppioni[2] | Arianna Menciassi[1] | Linda Paternò[1]

[1]The BioRobotics Institute and Department of Excellence in Robotics & AI, Sant'Anna School of Advanced Studies, Pisa, Italy | [2]Centro Protesi INAIL, Bologna, Italy

Correspondence: Maria Grazia Polizzotto (mariagrazia.polizzotto@santannapisa.it) | Linda Paternò (linda.paterno@santannapisa.it)

Received: 28 August 2025 | **Revised:** 1 January 2026 | **Accepted:** 4 January 2026

Keywords: amputations | compression therapies | McKibben actuators | mechanotherapy | pneumatic actuation | postoperative edema treatments | soft robotics | wearable robotics

ABSTRACT

Residual limb edema after amputation complicates rehabilitation and delays prosthetic fitting. This work presents a soft-robotic compression device for edema management in residual upper and lower limbs following amputation. Helically wound McKibben actuators (diameters of 5 and 8 mm; lengths of 50 and 100 cm) are embedded within a textile substrate and actuated sequentially to emulate manual lymphatic drainage. A wearable control unit allows sequential actuation. The actuators achieve strains of 26%–28% at 1.5 bar, with a maximum standard deviation of 0.60%, and deliver maximum forces ranging from 33 to 60 N. FEM simulations conducted on rigid cylindrical models representing limbs (8.5 and 15 cm diameter for arm and leg, respectively) predict peak interface pressures of 33–48 kPa (arm) and 21–32 kPa (leg), which are confirmed by benchtop experiments (37–45 kPa and 24–32 kPa for arm and leg, respectively). In vitro validation on high-fidelity residual limb simulators demonstrates therapeutic interface pressures of 5–11 kPa (upper limb) and 6–13 kPa (lower limb), consistent with values reported in the literature. These results demonstrate the system's potential as a highly customizable and effective solution for postoperative edema management, enabling personalized and at-home treatment.

1 | Introduction

In recent decades, soft wearable robots have gained growing attention in rehabilitation research, finding applications across a wide range of therapeutic areas. Among these, mechanotherapy (i.e., the application of mechanical stimuli on body tissues to exert forces that treat musculoskeletal injury [1], or blood and lymphatic disorders [2]) represents a particularly promising avenue. This is attributable to the intrinsic compliance, flexibility, and ability of soft robotic systems to conform safely to complex, dynamic anatomical shapes. These characteristics facilitate the precise, safe, and comfortable delivery of therapeutic forces, enabling treatments that are both personalized and capable of dynamic adaptation to patient-specific movements and physiological variations, thereby optimizing therapeutic efficacy [3–5].

Within circulatory disorders addressed by mechanotherapy, lymphedema is a chronic condition affecting an estimated 250 million people worldwide (3%–4% of the global population) [6]. It can be classified as either primary, a rare congenital condition, or secondary, which accounts for up to 90% of cases and is typically caused by surgery, radiation, or trauma. Lymphedema is characterized by the pathological accumulation of lymphatic fluid in the interstitial space, which in severe cases can reach volumes of several hundred milliliters to over 2 L [7]. This accumulation leads to progressive swelling, tissue fibrosis, skin thickening, and a heightened risk of recurrent infections. These complications can significantly impair mobility, limb function, and overall quality of life and in advanced stages may result in irreversible tissue damage or elephantiasis [8].

Traditional management of secondary lymphedema begins with an intensive phase lasting 4–6 weeks, involving daily short-stretch compression bandaging, structured exercise, and 1-h clinician-delivered manual lymphatic drainage (MLD) sessions, typically administered 3–5 times per week [9, 10]. Following this, patients transition to the maintenance phase, intended for long-term control through self-management. This phase can extend for months to years and involves continued use of custom-fitted graduated compression garments during the day and compression bandages at night, as well as therapeutic exercises. Conventional compression bandages deliver constant, static pressures, while graduated-pressure garments apply a decreasing gradient (typically 5–8 kPa distally, tapering to 2–3 kPa proximally [5, 11, 12]) to optimize fluid drainage toward the body's core [13]. However, passive compression garments and bandages have several limitations, including patient discomfort, challenges with independent donning and doffing, and, most critically, the limitation of delivering only a continuous, unchanging pressure over time. While this static compression can assist in managing limb volume by increasing interstitial pressure and facilitating passive venous and lymphatic return, it lacks the ability to actively mobilize fluid or promote dynamic flow. In contrast, clinician delivered MLD consists of gentle ($\sim$4 kPa), rhythmic pressure and sweeping motions from the distal toward proximal regions, effectively driving interstitial fluid toward central lymphatic pathways and achieving superior therapeutic outcomes [14]. On the other hand, MLD relies on specialized personnel, whose availability and accessibility may be limited for many patients. In this regard, active compression systems that replicate MLD dynamics offer a superior alternative to static garments by providing programmable, dynamic compression therapy capable of simulating rhythmic manual massage. These systems can be precisely tailored to patient-specific needs, enabling consistent, daily self-managed therapy, significantly reducing reliance on clinician-administered interventions [5].

The literature describes various active compression systems for circulatory disorders based on different soft actuation principles, including shape memory alloys (SMA) [15], shape memory polymers (SMPs) [16], and dielectric elastomer actuators (DEAs) [17]. However, pneumatic actuation remains the predominant approach in both research prototypes and commercial products (e.g., the Lympha Press system [18]), with pneumatic lymphatic drainage already offered to some patients during the maintenance phase of edema treatment [13]. Pneumatic actuators offer advantages such as design flexibility, high power-to-weight ratios (commonly exceeding 1 kW/kg for pneumatic artificial muscles [19]) simple control architectures, as well as enhanced operational safety compared with SMAs (which require activation temperatures around 90°C [20]), SMPs (which necessitate activation voltages ranging from 50 to 200 V and localized heating to reach transition temperatures between 40°C and 80°C [21]), and DEAs (which operate at high voltages, typically in the 1–5 kV range [22]). Primary limitations of pneumatic actuators—such as material fatigue, burst risk, the size and weight of control units—can be addressed through comprehensive materials characterization to ensure safe pressure operation, alongside the incorporation of recent more lightweight and compact micropumps and valves, which help reducing overall system size and weight. On the other hand, compression devices are designed for relatively short, home-based, or clinical treatment sessions, making extreme miniaturization and ultra-lightweight components less critical compared with other wearable robotics applications dedicated to daily life activities.

Different multichambered pneumatic devices have been proposed in the literature [23–25] many of which closely follow the architecture of commercially available intermittent pneumatic compression (IPC) systems. These devices typically rely on air bladders that, upon inflation, exert compression forces on the skin. While they are easy to fabricate and scale, their flat, welded, or bonded construction conforms poorly to limb geometries, often resulting in uneven pressure distribution during actuation. Their large internal effective volumes result in slow actuation cycles (typically $\sim$ 0.2 Hz), limiting system responsiveness, and lowers the overall efficiency. Moreover, they generally produce relatively low output forces, which can limit therapeutic effectiveness in certain applications. An alternative approach was introduced by Zhu et al. [26] using fluidic fabric muscle sheets (FFMS). This system consists of multiple thin elastic tubes (about 1 cm in diameter and 25 cm in length) wrapped entirely around the limb, enabling better conformity to anatomical geometry compared to bladder actuators and potentially providing more uniform interface pressure. The reduced actuator dimensions favor rapid interface pressure rises (exceeding 22 kPa at frequencies of 14 Hz and 160 kPa inlet pressure), which facilitates transiently elevated venous velocity, a desirable effect in compression therapy [27]. However, unlike conventional compression systems that apply interface pressure when inflated, the FFMS mechanism operates inversely: it provides passive compression on the limb when not actuated, while pressurization of the pneumatic actuators causes them to elongate, thereby reducing the pressure exerted on the skin by loosening the compression. Thus, compression is the default state, and actuation temporarily releases it. This operating principle may pose potential limitations, including reduced controllability and the need for active actuation to maintain a pressure-free state, which necessitates continuous system activation during donning or doffing of the device.

In this context, this study presents a novel design employing soft tubular actuators wrapped circumferentially around the limb, utilizing McKibben-type actuators that contract upon pressurization, exhibiting muscle-like behavior rather than elongation. This configuration facilitates the active generation of compression forces during actuation, thereby better aligning with the therapeutic objective of dynamically modulating interface pressure. To the best of our knowledge, no prior works have leveraged McKibben actuators in this circumferential configuration for wearable mechanotherapy. Driven by clinical and anatomical requirements, this implementation necessitates actuators of considerable length to ensure coverage of large residual-limb segments. To meet these requirements, McKibben actuators incorporating in-house silicone tubes at lengths of 50 and 100 cm were developed and characterized. Indeed, while previous studies have explored McKibben actuators at comparable lengths to our designs, they have primarily employed either commercial actuators (i.e., by FESTO Co. Ltd [28]) or commercial tubes as inflatable chambers (Table 1). These solutions are typically made from stiffer materials, which inherently limit design flexibility and device adaptability, and necessitate higher actuation pressures. In turn, such pressures require bulkier, heavier, and noisier control units, often making the system unsuitable for wearable or portable applications. To overcome these limitations and enable more customizable, low-pressure actuation, we fabricated in-house

TABLE 1 | Summary of the state of the art on the characterization of McKibben actuators with comparable lengths. The table highlights key parameters such as actuator length and materials used, providing context and comparison with the present work.

Reference	Length, cm	Material	P_{in}, bar
AKAGI et al. [29]	Up to 50	FESTO Co. Ltd	Up 3
Morita et al. [30]	50	Nitrile rubber	Up to 70
Uppalapati et al. [31]	50	Stretchable elastomer	Up to 1.40
Kurumaya et al. [32]	Up to 35	Silicone tube	Up to 3.50
Mori et al. [33]	70	Rubber tube	Up to 40
Mori et al. [34]	60	Rubber tube	Up to 40

actuators using very soft, compliant material (i.e., Ecoflex 00–30 silicone, Shore 0030, Smoothon-, Inc., Macungie, PA, USA).

McKibben actuators are well-known for their high force-to-weight ratio and good controllability compared with other soft pneumatic actuators [19]. With a high technology readiness level (TRL) and very good performance characteristics, they provide a solid foundation for pursuing real-world applications in soft robotics [35].

The proposed solution was developed specifically for managing postoperative edema in patients following limb amputation, as compression bandages and MLD are the only available interventions in this context. Although a few commercial devices are available [18], they typically feature a basic design, often limited to just a few pneumatic bladders, are not widely known, and are very rarely adopted in routine clinical practice. Edema management typically begins around 3 weeks post-amputation and may continue for several weeks to months, until limb volume stabilizes between 12 and 18 months post-amputation [36]. Post-amputation edema is the major cause of residual limb volume fluctuations during the early postoperative phase, with changes reaching up to 35%, that delay prosthetic fitting [36]. Thus, a solution capable of promoting effective edema reabsorption while dynamically adapting to these volume fluctuations is critical for timely rehabilitation and successful prosthetic integration, ultimately supporting the patient's reintegration into society [37, 38].

The proposed designstrategy is highly flexible, enabling easy customization to suit individual patient anatomy and variations over time, as well as therapeutic requirements. Owing to this flexibility, although initially developed for post-amputation edema, the proposed solution can be readily adapted for use in other lymphedema treatment contexts. In this work, two wearable systems designed and optimized for upper and lower residual limbs of standard sizes are presented. The devices integrate long, in-house-fabricated McKibben actuators embedded into a textile substrate and arranged in a helical configuration around the limb. These actuators are controlled via a custom unit that enables sequential inflation, effectively replicating the behavior of MLD therapy. This innovative approach aims to provide a practical, comfortable, and effective mechanotherapy solution that can be adapted to individual patient needs and used in everyday clinical and home settings.

2 | Results and Discussion

2.1 | Design Overview

An overview of the massage systems developed for treating postoperative edema in individuals with limb amputation is shown in Figure 1a. The system is a wearable soft robotic device built on a textile substrate, into which McKibben pneumatic actuators are embedded in a helical, sequential configuration. This layout closely conforms to the natural shape of the limb, minimizing gaps between actuators and thereby eliminating non-actuated regions that could be prone to fluid stagnation, as recommended by clinical experts. Two configurations were developed: one tailored for the upper limb and one for the lower limb, each optimized in terms of actuator number, size, and anchoring layout. As a textile substrate, the devices employ off-the-shelf prosthetic suspension sleeves, sized according to standard residual limb dimensions. An adjustable hook-and-loop belt is integrated into the sleeve to stabilize the device: it wraps around the waist for the lower-limb version and under the contralateral shoulder for the upper-limb version, ensuring consistent placement throughout treatment. Additionally, oversized fabric loops along the sleeve guide and stabilize actuator positioning while accommodating radial expansion during inflation.

The final design strategy yields a highly customizable yet modular architecture that can be readily adapted to a range of limb lengths, diameters, and soft tissue characteristics, while also allowing for straightforward actuator replacement when needed. The McKibben actuators were custom-fabricated in-house, enabling a simple and cost-effective manufacturing process, while ensuring a robust and reliable solution suitable for repeated use. By varying the diameter (D) and length (L) of individual actuators, it is possible to define localized compression zones of different sizes and then different pressure distributions along the limb (Figure 2). By combining multiple actuators, the system can support a wide range of programmable activation sequences, enabling multiple massage protocols tailored to specific therapeutic needs.

The actuators are driven by a compact wearable control unit (Figure 1b) that regulates inflation and deflation patterns via a pneumatic circuit composed of a micro diaphragm pump, solenoid valves, and pressure sensors. The control unit is housed in a 3D-printed enclosure (12 mm × 16 mm), designed for portability and belt mounting. The control unit supports both battery-powered and bench-top configurations. In its wearable version, the full system weighs ≈480 g for a configuration with one actuator, with an additional 25 g for each extra actuator. For the treatment of post-amputation edema, in alignment with recommendations from clinical experts, an activation strategy was implemented that delivers localized, progressive compression along the residual limb, following a distal-to-proximal massage pattern (sequential protocol in Figure 2). Specifically, each actuator inflates in sequence, holds

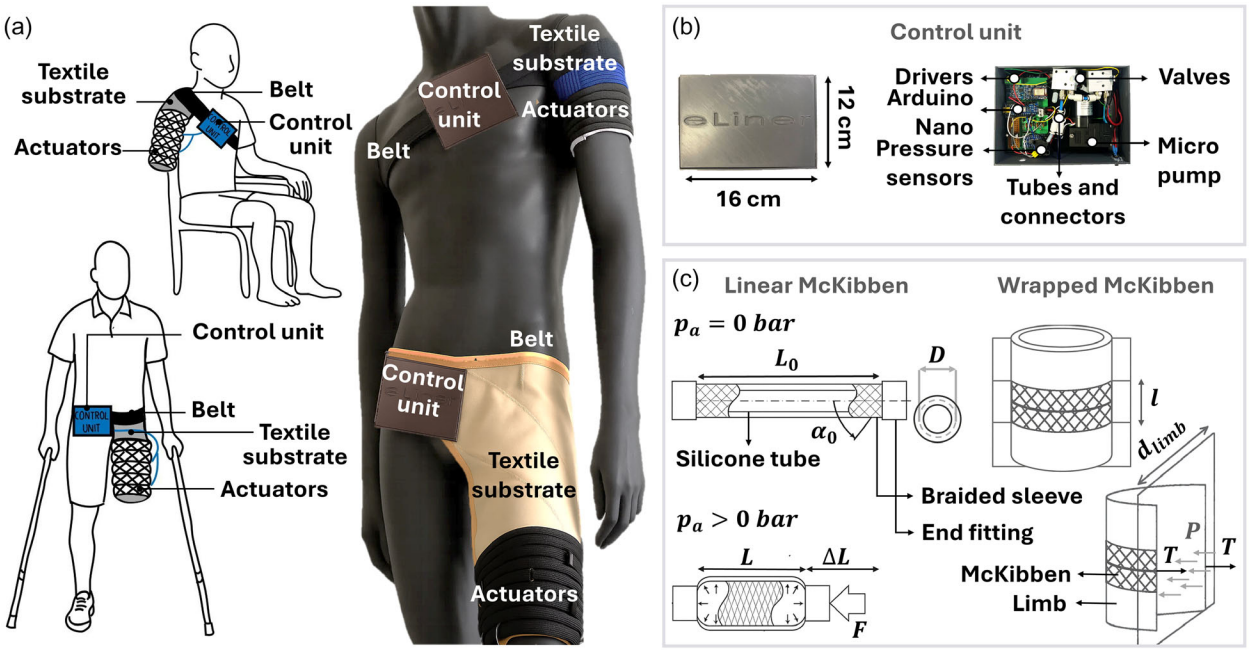

FIGURE 1 | (a) System overview of the wearable device for postoperative edema therapy in individuals with limb loss. The system consists of a textile substrate integrated with sequentially arranged McKibben pneumatic actuators, configured in a helical pattern around the limb. (b) A compact control unit, comprising an Arduino Nano, pressure sensors, valves, micropump, and connection tubing, regulates the inflation and deflation cycles of the actuators to deliver targeted compression. (c) Analytical model of linear and wrapped McKibben actuators showing axial contraction under inlet pressure in the linear configuration and radial compression around the limb in the wrapped configuration. L_0, actuator resting length; D, actuator mean diameter at rest; α_0: braid angle at rest; p_a, actuator inlet pressure; T, actuator axial force in the wrapped configuration; P, interface pressure; d_{limb}, average limb diameter, modeled as a cylinder.

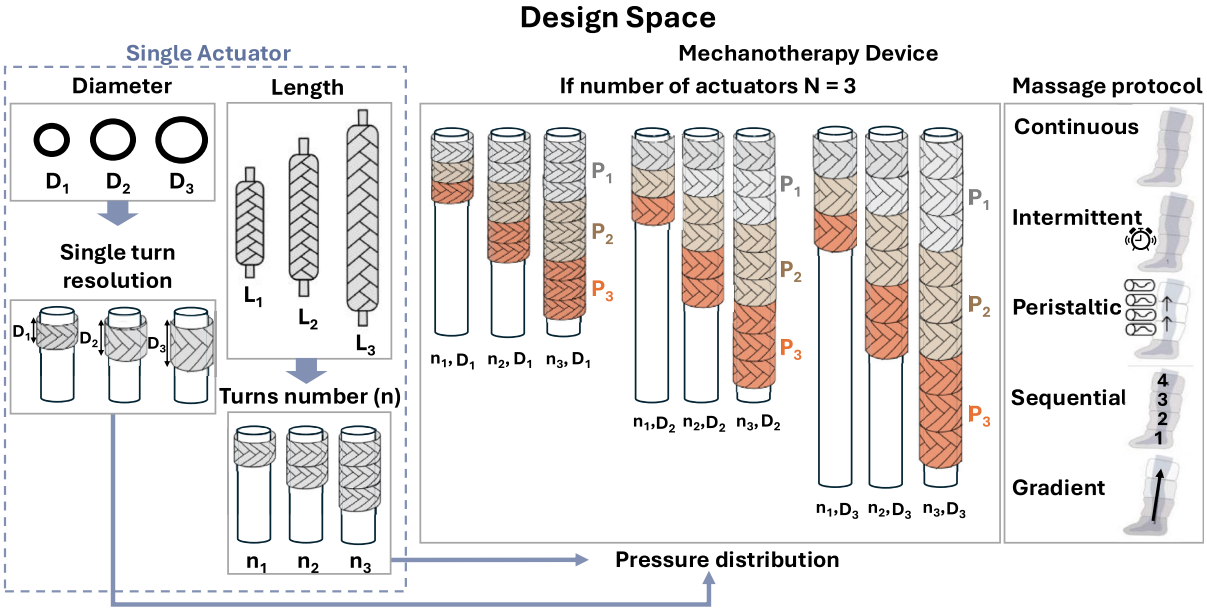

FIGURE 2 | Design space of the proposed wearable mechanotherapy device composed of McKibben pneumatic actuators. By varying the diameter (D) and length (L) of individual actuators, and their number of turns (n), it is possible to modulate the resolution of each compression zone and achieve different pressure distributions along the limb. Combining multiple actuators enables a range of programmable activation patterns, which in turn support multiple massage protocols, including uniform (uniform, constant interface pressure), intermittent (timely activation of uniform, constant pressure), peristaltic (wave-like sequential activation), sequential (each actuator deflates as the next inflates, from distal to proximal), and gradient (higher interface pressure distally, decreasing proximally) compression. This modular and customizable configuration allows for targeted and patient-specific therapeutic devices. Schematic of massage protocols was republished from [5] under the Creative Commons Attribution 4.0 International License (http://creativecommons.org/licenses/by/4.0/).

pressure briefly, and then deflates as the next actuator activates. Each full compression cycle is completed in less than 20 s. This approach is intended to promote interstitial fluid displacement and support lymphatic drainage. At the same time, the firmware remains fully configurable, allowing inflation/deflation timing and sequence to be tailored to individual patient needs, thus providing a customized therapeutic solution.

Quantitative data on interface pressure targets for mechanotherapy applications remain scarce and highly variable across the literature, with few studies specifically addressing the treatment of post-amputation limb edema [19, 22]. Reported compression levels delivered to residual limbs by pneumatic post-amputation assist devices are around 40 mmHg (≈5 kPa). However, pressure targets are often context-dependent and influenced by the specific patient population. A commonly referenced upper limit for safe compression in similar therapeutic settings is 60 mmHg (8 kPa) [5]. Due to the lack of systematic characterization and limited quantitative guidance specific to post-amputation edema management, we adopted this maximum reported value as a clinically relevant and conservative target in the design of our system. This approach ensures a safe starting point for therapy, while preserving the flexibility to adjust to lower pressure settings based on individual patient sensitivity and therapeutic response.

A basic model was used to derive indicative requirements for the forces and, in turn, for the actuator dimensions to achieve the target interface pressure. We assumed the residual limb as a cylindrical segment with an average diameter (d_{limb}) of 8.5 cm for the upper limb [39] and 15 cm for the lower limb [40] (Figure 1c). The axial force (T) exerted by the McKibben actuators to generate an interface pressure (P) is then calculated as:

$$T = \frac{PA}{2} = \frac{P d_{\text{limb}} Dn}{2} \tag{1}$$

where A is the cross-sectional area of a generic limb segment, modeled as a rectangle with width equal to the limb diameter d_{limb} and height $l = D\ n$, corresponding to the axial length covered by a single McKibben actuator of diameter D wrapped n times around the limb (Figure 1c). The standard force equation for a McKibben actuator relates its initial mean diameter (D), internal pressure (p_a), initial braid angle (α_0), and strain (ε) as [41]:

$$F = \frac{p_a \pi D^2}{4 \sin^2\ \alpha_0} \left[3 \cos^2\ \alpha_0 (1-\varepsilon)^2 - 1\right] \tag{2}$$

Considering D as the average of the silicone tube's inner diameter and the actuator's outer diameter (Figure 1c), approximating $T = F$ and solving for D yields:

$$D = \frac{2P\, n\, d_{\text{limb}} \sin^2\ \alpha_0}{\pi\, p_a [3 \cos^2\ \alpha_0 (1-\varepsilon)^2 - 1]} \tag{3}$$

We adopted a braid angle α_0 of 29° and a strain ε of 0.25, consistent with values reported in the literature [42, 43]. The internal pressure p_a was set to 1.5 bar, which corresponds to half of the maximum pressure deliverable by the wearable micro-pump, ensuring a safety margin, preserving component lifespan, and reducing power consumption during operation. Assuming a representative helical arrangement with $n = 2$ turns, actuator mean diameters of approximately 5 and 8 mm were estimated for upper and lower limb configurations, respectively. We selected $n = 2$ as a compromise: with $n = 1$, the design would require many more actuators to cover the same surface area, each with its own pneumatic line, fittings, valves, and electronic drivers, and this would substantially increase system complexity, weight, and the risk of air leakage, whereas with $n = 3$ the discretization of pressure along the limb—especially in the upper limb—would have already been partially lost. In consistency with this configuration and the assumed limb circumferences, we fabricated actuators in two lengths: 50 and 100 cm, respectively.

2.1.1 | McKibben Actuators

2.1.1.1 | Manufacturing. In the literature, the fabrication of custom silicone tubes is typically carried out using either roll coating [44] or molding techniques. However, roll coating presents significant challenges in maintaining uniform thickness, especially over extended lengths. Such non-uniformities increase the risk of bubble formation, mechanical failure, and asymmetric actuator behavior. For these reasons, the molding technique was preferred, as it enables more precise control over geometry, ensuring uniform wall thickness, structural integrity, and reliable actuator performance (Figure 3 and Supplementary Video 1). During fabrication, liquid silicone was injected into the mold using syringes. The considerable back-pressure along the full length of the cavity made the process challenging, so additional injection sites were strategically integrated into the mold to ensure full filling and eliminate trapped air. Based on manufacturing trials aimed at optimizing the balance between structural integrity, flexibility, and ease of fabrication, we selected a 2 mm tube wall thickness for all silicone tubes. The final mold was fabricated using Delrin, a material selected for its ability to prevent silicone adhesion, thereby facilitating demolding. Commercial braided sleeves were thermoformed to reduce the initial braid angle (α_0), aiming for values around 29°, and then assembled on silicone tubes using 3D-printed end fittings and commercial clamps. A digital microscope (HRX-01, Hirox USA Inc.) was used to acquire high-resolution images of the braided sleeves and to determine the initial resting braid angle (α_0) in each actuator (Table 2). The angle was measured at three positions along each actuator (top, middle, and bottom), and the average value was reported for each dimension. Table 2 shows that the 8 mm-diameter, 50 cm-long actuators exhibited higher mean braid angles (35.65 ± 5.8°) compared with the other configurations. This larger deviation is likely attributable to fabrication-related variability, particularly during the thermoforming process in which the sleeve is stretched and subsequently fixed onto the silicone tube.

2.1.1.2 | Characterization Tests in the Linear Configuration. Strain–pressure, isotonic, and isobaric tests were performed to systematically assess the performance of the actuators in a linear configuration using an Instron testing machine. The experimental setup included an air compressor (model JUNIOR 30, ABAC), an electronic proportional microregulator (Series K8P, Camozzi Group S.p.A., Milano, IT), and a digital pressure sensor (Series SWCN, Camozzi Group S.p.A., Milano, IT). All tests were repeated five times for each

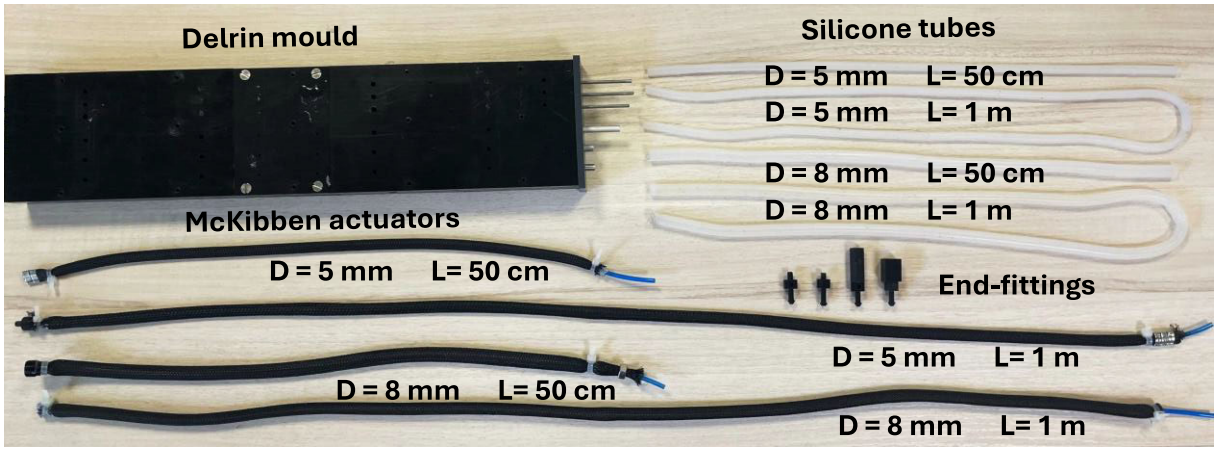

FIGURE 3 | Fabrication components and final prototypes of McKibben actuators in different dimensions. The image shows the Delrin mold used to fabricate custom silicone tubes, four silicone tubes (diameters of 5 and 8 mm, each produced in 50 and 100 cm lengths), and the corresponding assembled McKibben actuators. Actuators were completed using thermoformed braided sleeves, 3D-printed end fittings, and commercial clamps to ensure secure sealing and consistent performance.

TABLE 2 | Average initial braid angle (α_0) for actuators with different dimensions. Each value corresponds to the mean and standard deviation of angles measured at three locations along the actuator body. Mean diameter (D), inner diameter (D_{in}), and total actuator length (L) are reported, along with the number of actuators tested (N). All actuators are fabricated using silicone tubes with a wall thickness of 2 mm.

D, mm	D_{in}, mm	L, cm	$N°$	Angle, deg
5	3	50	3	29.76 ± 4.6
5	3	100	3	29.08 ± 6.0
8	6	50	3	35.65 ± 5.8
8	6	100	3	29.10 ± 5.5

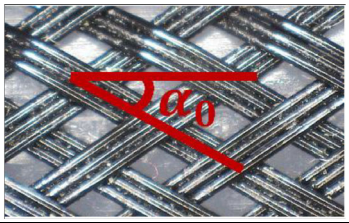

McKibben actuator, with three actuators tested per configuration. Strain–pressure characterization was performed using a quasi-static cyclic protocol. Each McKibben actuator was fixed at the upper end of an Instron testing machine and left free to contract at the opposite end, then subjected to incremental pressure steps. Pressure was manually increased in discrete steps of 0.1 bar, starting from 0 up to 1.5 bar, and then decreased back to 0 bar to complete a full cycle. At each pressure step, the actuator was allowed to stabilize before its length was recorded. Axial strain (ε) was calculated as $\varepsilon = |\Delta L|/L_0$, where $\Delta L = L_0\text{-}L$. Isometric tests involved increasing and subsequently decreasing the inlet pressure from 0 to 1.5 bar, in 0.25 bar steps, while measuring the output force under constant strain conditions. Specifically, each actuator was held at predefined strain levels (ε), ranging from 0% to 25% of its resting length, in 5% increments. Cyclic isobaric tests were conducted by applying seven fixed pressure levels (0 to 1.5 bar in 0.25 bar increments). At each level, the actuator was stretched back to its initial resting length (deformation rate: 60 mm/min), and the corresponding reaction force was recorded using the Instron load cell.

The strain–pressure tests demonstrated that all actuators achieved axial strains in the range of 26% to 28% at 1.5 bar inlet pressure, with a maximum standard deviation of 0.60% which reflects the high consistency and repeatability of actuator behavior (Figure 4b). Notably, longer actuators exhibited slightly higher strain compared to their shorter counterparts. For instance, the 8 mm × 100 cm actuators reached a strain of 27.94 ± 0.12%, while the 8 mm × 50 cm actuators showed a slightly lower strain of 27.05 ± 0.17%. The maximum standard deviations in strain were 0.60% for the 100 cm actuators and 0.38% for the 50 cm ones. A similar trend was observed for the 5 mm variants, where the 100 cm actuators reached a strain of 27.44 ± 0.10% and the 50 cm ones reached a strain of 26.19 ± 0.18%. The maximum standard deviations in strain were 0.29% for the 100 cm actuators and 0.57% for the 50 cm ones. This difference in the performance of 50 cm versus 100 cm long actuators can be attributed to the initial braid angle (α_0) of their sleeve and to the fact that, in longer actuators, the end fittings account for a smaller relative proportion of the overall length, thus having a less significant influence compared with shorter McKibben actuators [34].

Additionally, hysteresis remained relatively low across all configurations. The highest average hysteresis was observed in the 5 mm × 50 cm actuator (3.34%), while the lowest occurred in the 8 mm × 50 cm actuator (1.90%), which also had the highest initial braid angle. For the 100 cm-long actuators, comparable values were recorded: 2.94% for the 5 mm diameter and 2.65% for the 8 mm diameter. These results suggest that the observed energy losses could be influenced by the actuator's geometry. However, given the small hysteresis values, it is more plausible that the main source of variation arises from fabrication-related variability.

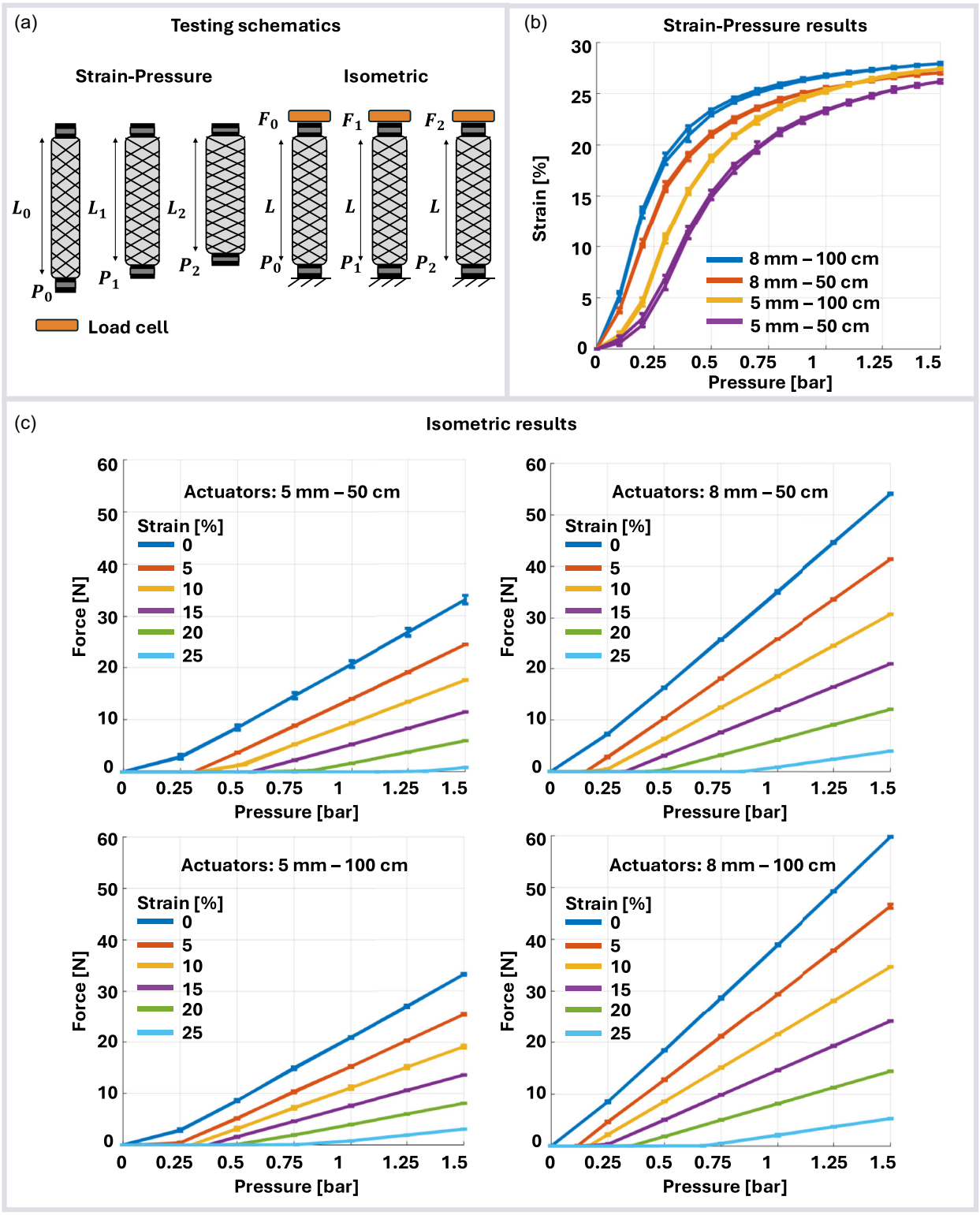

FIGURE 4 | Schematics (a) and results (b and c) of strain-pressure and isometric tests. (b) The strain-pressure plot shows actuator strain as a function of inlet pressure. (c) The isometric plots display actuator output force as a function of inlet pressure at fixed strain levels (0%, 5%, 10%, 15%, 20%, and 25%) for actuators with 5 mm diameter (left), with lengths of 50 cm (top) and 100 cm (bottom) and actuators with 8 mm diameter (right), with lengths of 50 cm (top) and 100 cm (bottom).

Isometric testing showed that 5 mm diameter actuators with lengths of 50 and 100 cm produced mean maximum forces of 33.09 ± 0.81 N and 33.23 ± 0.19 N, respectively, at 1.5 bar and 0% strain (Figure 4c). The maximum standard deviation in force was 0.81 N for the 50 cm actuators and 0.35 N for the 100 cm ones. Actuators with an 8 mm diameter generated 54.08 N ± 0.13 N (50 cm) and 59.76 N ± 0.09 N (100 cm). The maximum standard deviation in force was 0.22 N for the 50 cm actuators and 0.38 N for the 100 cm ones. As expected from Equation (2), an increase in the diameter D leads to higher force output, due to the quadratic dependence of the output force

on D. The small discrepancy in force between the two 8 mm actuators is likely attributable to differences in the braid angle α_0. Specifically, a lower α_0 increases $\cos \alpha_0$ (thus raising the numerator of the force equation) and decreases $\sin \alpha_0$ (reducing the denominator), resulting in a larger overall force. At the same time, using Equation (2) to estimate the output forces results in significantly lower theoretical values compared to the measured ones, likely due to model simplifications.

Isobaric testing at 1.5 bar inlet pressure showed that actuators with 5 mm diameter produced mean maximum forces of 33.30 ± 0.69 N (50 cm) and 35.88 ± 3.18 N (100 cm) (Figure 5). The maximum standard deviations in force were 1.28 N for the 50 cm actuators and 3.23 N for the 100 cm ones. The 8 mm diameter actuators generated mean maximum forces of 55.85 ± 8.24 N (50 cm) and 61.32 ± 6.43 N (100 cm) at 1.5 bar. The maximum standard deviation in force was 8.24 N for the 50 cm actuators and 6.43 N for the 100 cm ones. The force outputs closely match those obtained from the isometric tests; however, the isobaric protocol showed greater cycle to cycle variability, likely due to the dynamic variation in actuator length throughout

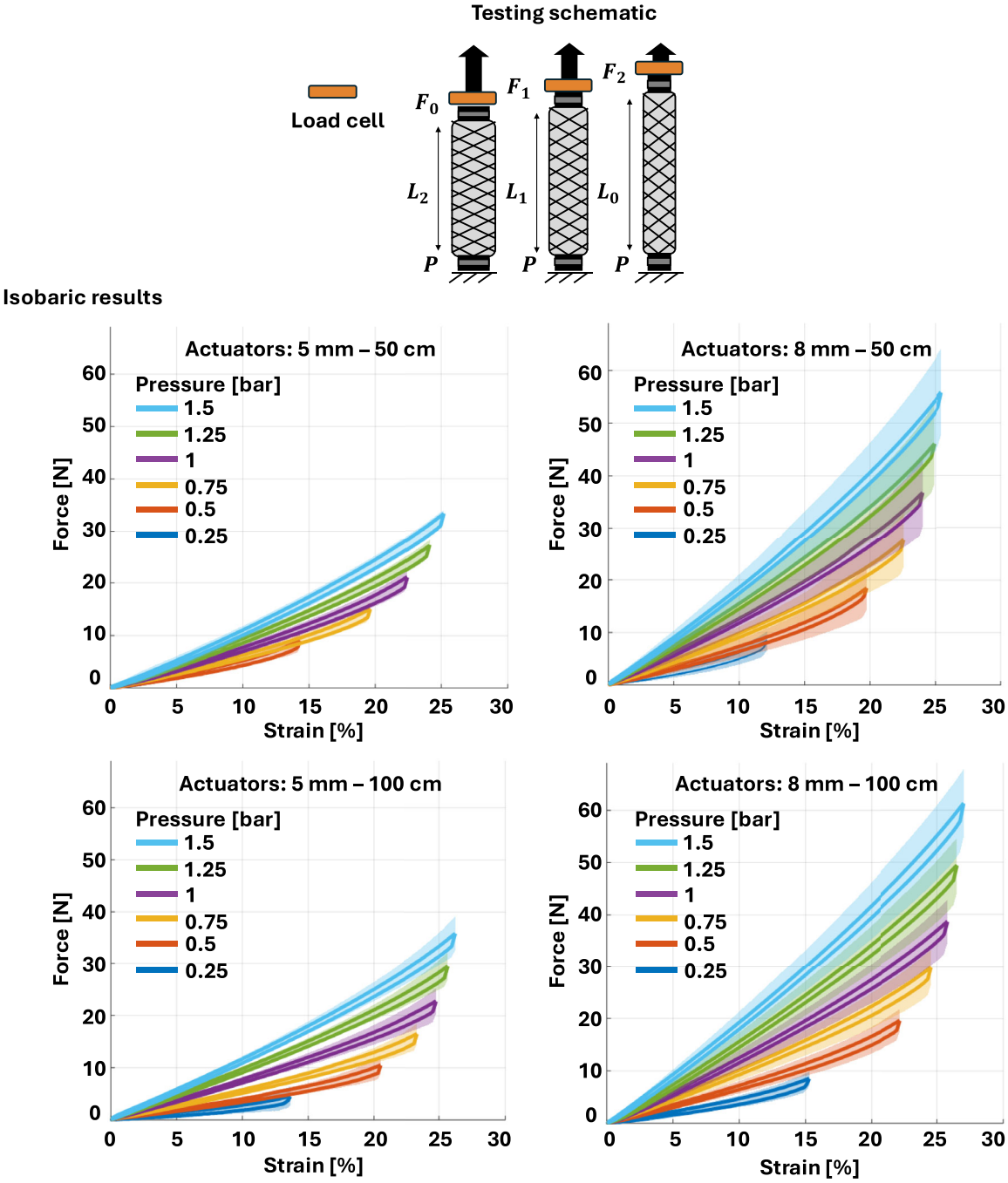

FIGURE 5 | Testing schematic and results of the isobaric tests. The plots show actuator output force as a function of strain levels at fixed inlet pressure (0.25, 0.5, 0.75, 1, 1.25, and 1.5 bar) for actuators with 5 mm diameter (left), with lengths of 50 cm (top) and 100 cm (bottom), and actuators with 8 mm diameter (right), with lengths of 50 cm (top) and 100 cm (bottom).

the cycles and the more pronounced effect of the silicone tubes' hyperelastic behavior.

2.1.1.3 | FEM Simulations. After completing the full characterization of the actuators in a linear configuration, nonlinear finite element method (FEM) simulations were conducted using Abaqus CAE/Explicit (Dassault Systèmes, Vélizy-Villacoublay, France) to evaluate actuator performance in their final helical configuration. These simulations were developed to overcome the limitations of the initial analytical model, which, despite its simplifications, was useful for providing first-order estimates of actuator dimensions and guiding the design space exploration. To model the behavior of the actuators while avoiding the complexity and high computational cost associated with fluid–structure interaction models or explicit meshing of the braid architecture, we adopted a simplified equivalent thermal loading approach, as described in [45]. This modeling strategy provides a computationally efficient alternative, while still capturing the anisotropic contraction and axial shortening characteristic of McKibben actuators, making it a particularly suitable solution for simulating the actuators in the target helical wrapping configuration. To achieve an accurate representation of the actuator behavior, orthotropic thermal expansion coefficients were introduced to ensure proper longitudinal contraction and radial expansion, thereby effectively replicating the experimentally observed mechanical response to internal pressurization through temperature control. To estimate the maximum interface pressure exerted during operation, the actuators were modeled as solid cylindrical tubes wrapped around cylinders with diameters of 8.5 and 15 cm, representing the geometries of the upper and lower limbs, respectively.

Specifically, 50 cm-long actuators with diameters of 5 and 8 mm were wrapped around the arm cylinder (8.5 cm), while 100 cm-long actuators with the same diameters were wrapped around the leg cylinder (15 cm). Although the 8 and 5 mm actuators were originally intended for leg and arm applications respectively, both were tested in each configuration to enable a more comprehensive characterization and to assess scalability and performance consistency across different limb sizes. Each actuator was modeled as a solid helical cylinder wrapped around the limb-representative cylinders, which were themselves modeled as discretely rigid hollow cylinders (to reduce computational cost while still enabling extraction of the actuator–surface contact pressure). The actuators were assigned with isotropic properties matching Ecoflex 00–30 (elastic modulus 0.125 MPa [46]). In addition, three distinct thermal coefficients were imposed: εx and εy were set to 50% to capture the actuator's radial expansion, while εz was set to 25% to reproduce its axial contraction. All coefficient values were derived from experimental measurements obtained at the maximum pressure of 1.5 bar. All three coefficients were defined as functions of a prescribed temperature increase of 1°C, which was used as an equivalent representation of the experimentally observed internal pressurization and applied as a "Load". This increase is defined as a function of time, thereby enabling a temporal analysis of the contraction, and allowing its evolution to be assessed every instant.

The mesh comprised linear tetrahedral elements (C3D4 type) with a characteristic length of 1 mm. The rigid cylinder and both actuator ends were fixed in space in all three rotations and translations, with a fixed constraint (6 degrees of freedom). A general contact interaction was defined between the outer surface of the actuator and the surface of the cylinder.

A dynamic explicit analysis was run over 1 s with a minimum time increment of 10^{-4} s.

Simulations results were analyzed in terms of contact pressure between the actuators and cylinder surfaces (Supplementary Video 2). The values were extracted at the point of maximum actuator contraction. For each simulation, the maximum interface pressure and the mean interface pressure were obtained (Table 3). The simulations results show that the mean contact pressures are substantially lower than the corresponding peak pressures. This discrepancy can be attributed to the heterogeneous nature of the actuator–cylinder interface, as well as to the limited ability of the model to accurately capture contact behavior during deformation: localized regions of poor contact produce very low-pressure readings that pull down the overall average. At the same time, in areas where proper contact was modeled, the predicted peak pressure values showed good agreement with experimental measurements, as confirmed in subsequent testing. Indeed, experimental validation was then performed under the same conditions used in the simulations.

2.1.1.4 | Characterization Tests in the Helical Configuration. The actuators were wrapped in two full turns ($n = 2$) around two 3D-printed rigid cylinders, with diameters of 8.5 and 15 cm, corresponding to the upper- and lower-limb configurations, respectively. TekScan pressure sensors (9833E pressure sensors of the F-Socket System, Tekscan Inc., Boston, MA) were positioned at the actuator–cylinder interface to acquire contact pressure data throughout three consecutive inflation trials (Figure 6). During each trial, the actuators' internal pressure was increased in 0.25 bar increments at 10 s intervals, from 0 up to 1.5 bar and the relationship between inlet actuator pressure and interface pressure was plotted (Figure 6). Actuators measuring 50 cm in length (with diameters of 5 and 8 mm) were tested on the cylinder representing the upper limb, while 100 cm long

TABLE 3 | Simulation results showing the peak and mean interface pressures generated by a single actuator wrapped twice around a rigid cylinder representing the dimensions of the upper and lower limbs.

Rigid cylinder diameter, cm	Actuator diameter, mm	Actuator length, cm	Max interface pressure, kPa	Mean interface pressure, kPa
8.5	5	50	33.8	23.3
8.5	8	50	48.3	33.5
15	5	100	21.2	8.6
15	8	100	31.9	15.8

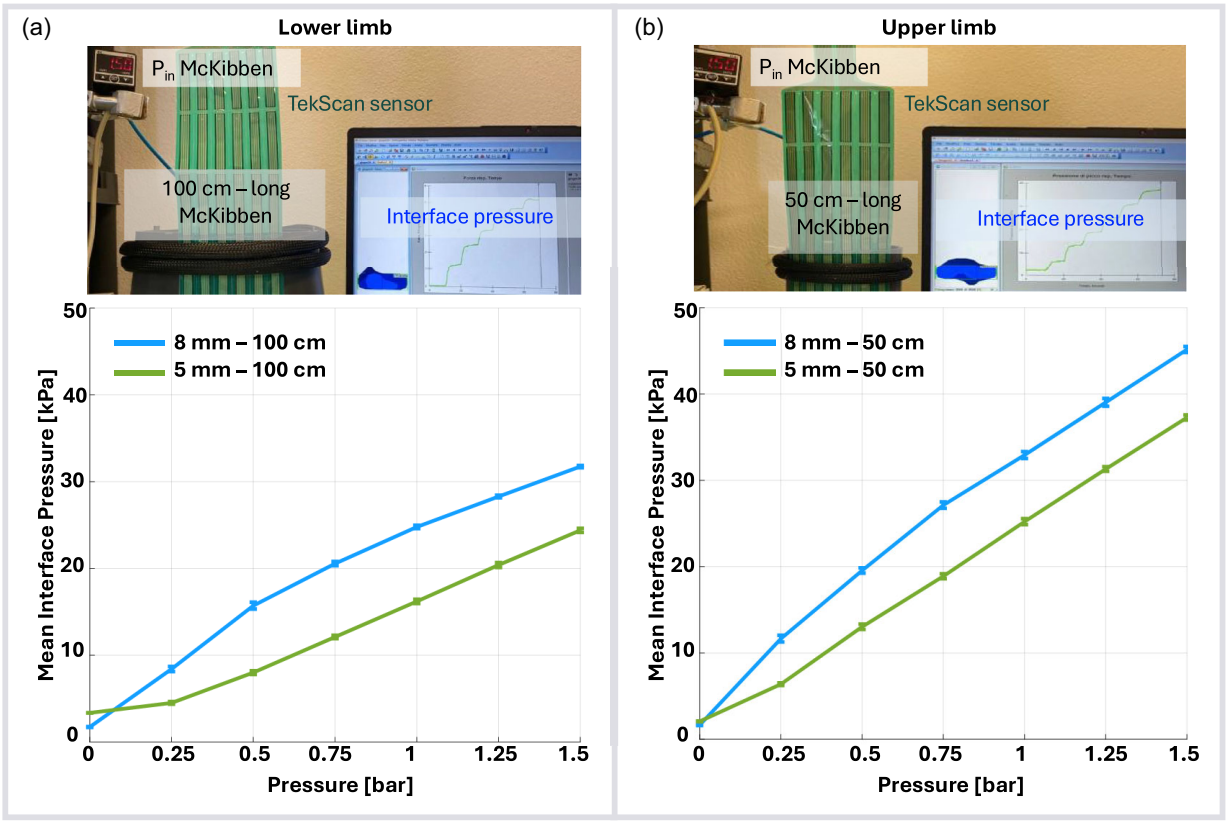

FIGURE 6 | Experimental setup (top) and representative results (bottom) of the McKibben actuator characterization tests in the final helical configuration wrapped around rigid cylindrical limb models: (a) lower-limb cylinder and (b) upper-limb cylinder.

actuators with the same diameters were tested on the cylinder representing the lower limb.

Results showed that 50 cm-length actuators wrapped around the 8.5 cm diameter cylinder produced mean interface pressures of 37.28 ± 0.29 kPa (5 mm diameter) and 45.16 ± 0.35 kPa (8 mm diameter), with maximum standard deviation across the entire test of 0.34 and 0.46 kPa, respectively. In contrast 100 cm-long actuators, wrapped around the 15 cm diameter cylinder produced mean interface pressure of 24.40 ± 0.23 kPa (5 mm diameter) and 31.74 ± 0.13 kPa (8 mm diameter), exhibiting maximum standard deviations of 0.28 and 0.39 kPa, respectively. Although actuators of the same diameter but different length generate very similar maximum forces in the linear configuration (Figures 4 and 5), the helical-configuration measurements revealed differences in interface pressure, due to variations in contact area. As expected, distributing the same axial force over a smaller contact area resulted in higher interface pressures. This was observed with the 50 cm-long actuators wrapped around the upper-limb cylinder, compared to the actuator of the same diameter but 100 cm in length wrapped around the lower-limb cylinder.

The obtained experimental results are in good agreement with the maximum interface pressure of FEM simulations, validating the accuracy of the modeling approach. Specifically, for the 50 cm-long actuators wrapped around the upper-limb rigid cylinder, experimental values of 37.28 ± 0.29 kPa and 45.16 ± 0.35 kPa closely matched the simulated values of 33.8 and 48.3 kPa for 5 and 8 mm diameters, respectively. Similarly, for the 100 cm-long actuators on the lower-limb cylinder, measurements of 24.40 ± 0.23 kPa and 31.74 ± 0.13 kPa were consistent with the predicted 21.2 and 31.9 kPa for 5 and 8 mm diameters, respectively. The slightly lower values observed in the FEM simulations may be attributed to idealized assumptions in material behavior and contact definitions, including frictionless interfaces and uniform expansion.

Although these interface pressures exceed the target therapeutic threshold of 8 kPa, it is important to note that these tests were performed on rigid cylindrical substrates, which were selected to enable repeatable and controlled characterization of the maximum interface pressure capability of the actuators in the final helical configuration. In realistic conditions, when the actuators are applied to compliant, soft tissue substrates, lower interface pressures are expected due to material deformation and load distribution, aligning more closely with clinical requirements.

2.1.2 | Wearable Control Unit

The control unit of the system is a custom-built platform designed around an Arduino Nano microcontroller (weight: 6 g) and can be powered either by a lithium-ion battery (PICPALNB27, Panasonic, weight: 220 g) for fully wearable operation or by an AC/DC transformer (IRM-60-12ST, MEAN WELL, weight: 206 g) for bench-mounted use (Figure 1b). It incorporates a compact pneumatic circuit centered on a DC brushless microdiaphragm pump (NMP830.1.2KPDC-B4 HP, KNF DAC GmbH, max. operating pressure, 3 bar g; flow rate, 9 l/min; weight 220 g) with an acoustic silencer (KNF DAC GmbH, weight: 7 g).

For each McKibben actuator, the unit integrates two miniature solenoid valves, one 2/2 normally closed and one 3/2 normally open (Series K8, Camozzi, weight: 7 g each), along with a pressure sensor (MPX5700DP, NXP semiconductors, pressure range, 0–700 kPa; weight, 5 g) for continuous pressure monitoring and enforcement of a 1.5 bar safety limit. A dedicated motor driver module (HG7881, weight: 6 g) manages valve actuation. The entire system is housed in a 3D-printed enclosure (dimensions: $12 \times 16 \times 6\ cm^3$) featuring a rear mounting tab for attachment to the belt harness of the device.

The microdiaphragm pump is connected to a custom pneumatic manifold, with one outlet per actuator. Each outlet feeds a 2/2 valve whose output connects to a 3/2 valve; the remaining ports of the 3/2 valve serve as the inlet and exhaust of the actuator. During operation, the pump activates and the 2/2 valve corresponding to the most distal actuator opens, allowing airflow through the normally open port of the 3/2 valve into the McKibben chamber, initiating inflation. Once the target pressure is reached, the 2/2 valve closes, maintaining the actuator in its contracted state. The 3/2 valve then vents the actuator through its exhaust port. As the distal actuator deflates, the next actuator in the proximal sequence inflates, continuing the sequential compression cycle along the limb.

2.2 | In Vitro Validation

The final devices were validated in vitro using high-fidelity upper- and lower-limb residual simulators, constructed from soft materials that replicate the mechanical properties of human soft tissue and equipped with internal fluidic chambers designed to mimic postoperative edema conditions (Figure 7) [47, 48]. Specifically, two mechanotherapy devices incorporating five McKibben actuators were developed for the lower-limb simulator, and two mechanotherapy devices incorporating three actuators were developed for the upper-limb simulator. As in previous tests, both 8 and 5 mm diameter actuators were evaluated in each configuration, using 50 cm actuators for the upper limb and 100 cm for the lower limb, to enable a more comprehensive characterization and assess scalability and performance consistency across different limb sizes. The operation of systems using 8 mm diameter, 100 cm long actuators for the lower limb and 5 mm diameter, 50 cm long actuators for the upper limb is demonstrated in Supplementary Video 3 (Figure 7). The control strategy was informed by feedback from a focus group with clinical experts and was designed to deliver a distal-to-proximal sequential massage cycle over the residual limb, with each full cycle completed within 20 s. Using the wearable control unit, the actuators are pressurized in sequence: as one actuator begins to deflate, the next inflates immediately, generating a continuous wave of compression along the limb. This timed overlap between deflation and inflation ensures smooth pressure propagation, promoting interstitial fluid displacement and enhancing lymphatic drainage, in line with therapeutic recommendations.

During in vitro validation, the first test involved driving each actuator at its maximum operating pressure of 1.5 bar, while interface pressures were continuously monitored using Tekscan sensors placed between the textile sleeve and the simulator surface, with the fluid chamber kept empty. All actuators in the upper-limb device were activated during the massage sequence. In contrast, in the lower-limb configuration, only the three most proximal actuators were activated, corresponding to the position of the embedded fluidic chamber in the upper section of the leg simulator, consistent with the experimental setup

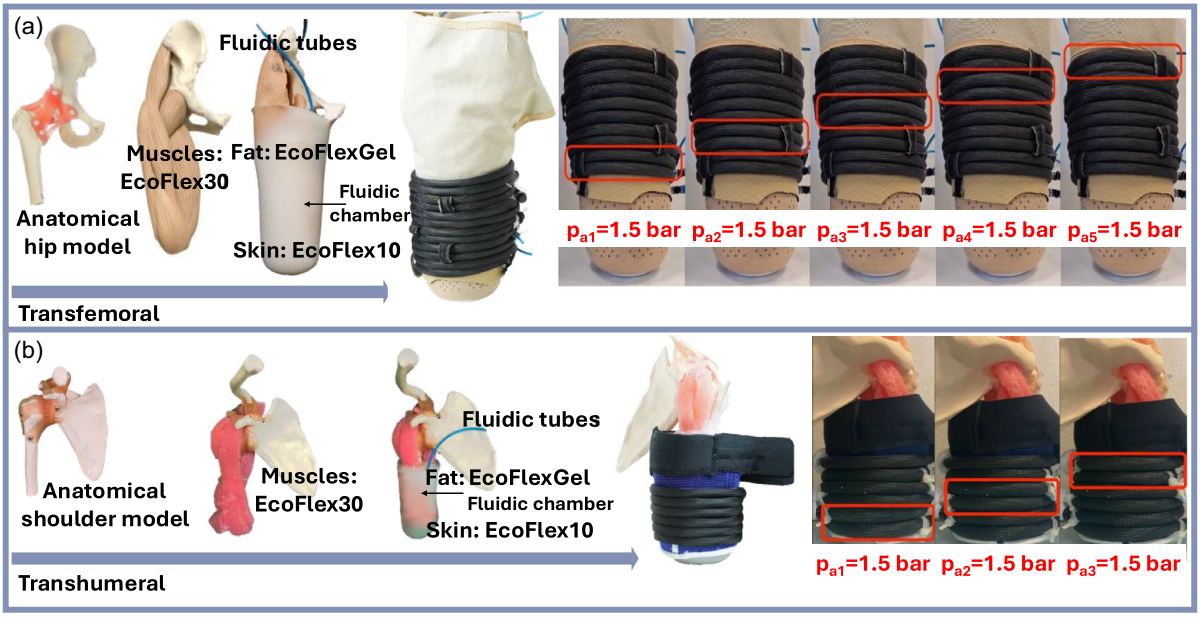

FIGURE 7 | Wearable soft robotic devices designed for mechanotherapy applications, fitted onto high-fidelity residual limb simulators representing (a) transfemoral and (b) transhumeral amputations. The simulators replicate the mechanical properties and anatomical structure of bone, muscles (Ecoflex 30 silicone), fat (Ecoflex Gel), and skin (Ecoflex 10), incorporating embedded fluidic chambers to simulate bodily fluid accumulation. On the right, photographs show the actuation sequence with pressures applied to each actuator (highlighted by red boxes), illustrating the progressive inflation cycles employed during in vitro validation to mimic therapeutic massage protocols.

described later in the manuscript. Pressure data were acquired over four cycles for each actuator, and the mean and standard deviation across cycles were plotted. The pressure traces shown in Figure 8 illustrate the sequential activation of the three actuators for each cycle, with each deflation coinciding with the inflation of the next.

These tests demonstrated that both devices achieved interface pressures approaching or exceeding the commonly referenced therapeutic target of up to 8 kPa reported in the literature. As shown in Figure 8, the upper-limb wearable device generated interface pressures between 5 and 8 kPa when actuated by 5 mm × 50 cm actuators, aligning with the target, and pressures of 9–11 kPa with 8 mm × 50 cm actuators, slightly exceeding the typical therapeutic range. For the lower-limb device, 5 mm × 100 cm actuators produced interface pressures of 6–8 kPa, aligning with the target, while 8 mm × 100 cm actuators reached pressures between 10 and 13 kPa, surpassing the expected therapeutic levels. Slight differences in mean pressure applied by different actuators of the same device can also be attributed to the fact that the two simulators were fabricated from scans of real residual limbs, replicating their natural shape and thus exhibiting non-uniform circumferences and irregular geometries, to which the Tekscan sensors cannot perfectly conform.

From these experimental results, it is also possible to see that each of the 50 cm modules completed an inflation–deflation cycle in ≈3 s (5 mm) and 4 s (8 mm), while each of the 100 cm modules required about 5 s (5 mm) and 7 s (8 mm). Consequently, sequencing three modules distally to proximally yields a full massage cycle in under 20 s, meeting the cycle-time recommendations of clinical specialists.

Subsequently, in vitro validation included tests in which the simulators' fluidic chambers were filled with 80 mL of colored water for the lower-limb device and 10 mL for the upper-limb device, to simulate interstitial fluid accumulation (Figure 9). The tests employed 5 mm diameter, 50 cm long actuators for the upper-limb system and 8 mm diameter, 100 cm long actuators for the lower-limb system. Each actuator was sequentially driven at its maximum operating pressure of 1.5 bar, while interface pressures were continuously monitored using Tekscan sensors. As shown in Supplementary Video 4, in both cases, fluid was propelled from the distal to the proximal end of the residual limb simulators, effectively achieving the therapeutic goal of post-operative edema massage therapy. The lower-limb device expelled 33.65 mL (corresponding to 42.06% of the 80 mL injected) against gravity in 7 cycles; the upper-limb device expelled 6.50 mL (corresponding to 65% of the 10 mL injected) against gravity in five cycles. Although fluid continued to be ejected beyond these cycle counts, the flow rate decreased markedly, transitioning from a continuous stream to a slow, intermittent droplet release.

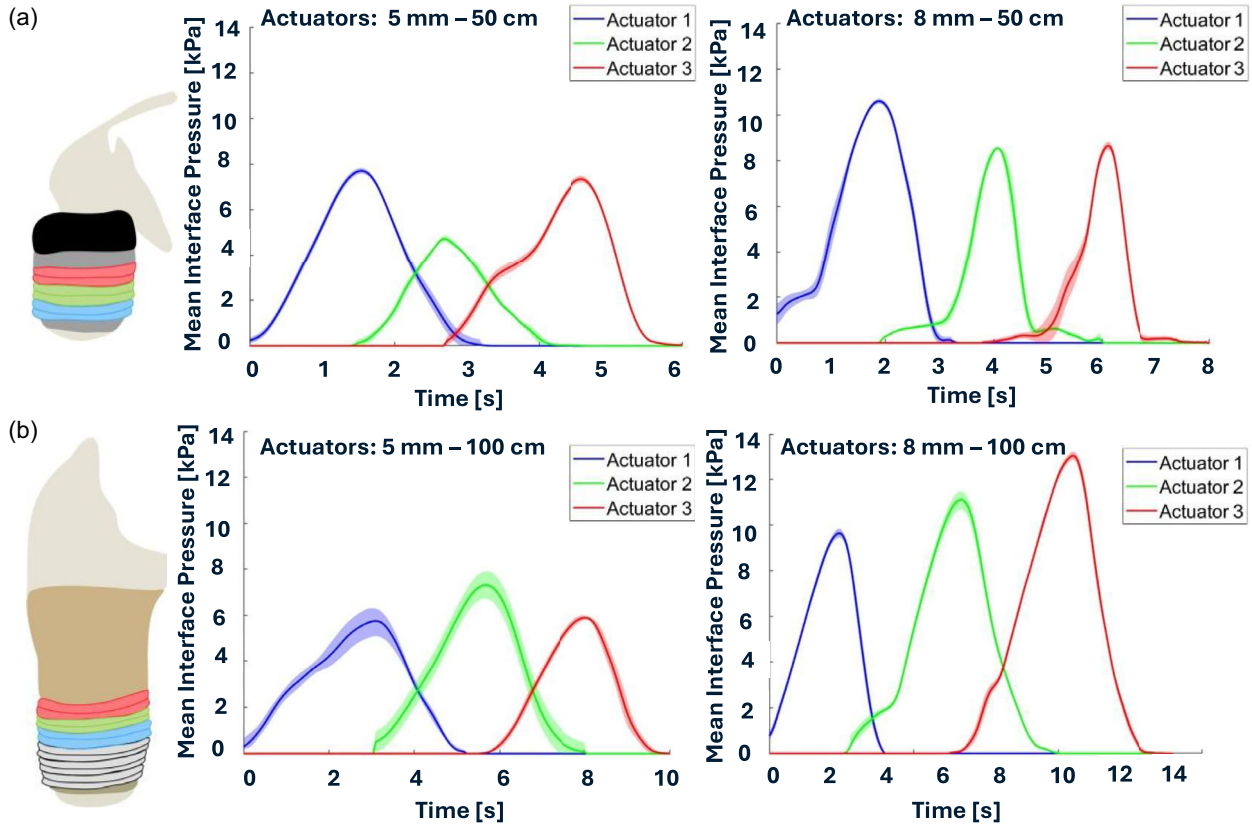

FIGURE 8 | Mean interface pressure profiles over time recorded from three sequentially actuated McKibben actuators embedded in wearable mechanotherapy devices for (a) upper-limb and (b) lower-limb simulators. The left column shows results for actuators with 5 mm diameter, while the right column presents data for 8 mm diameter actuators. Upper panels correspond to 50 cm-long actuators, and lower panels to 100 cm-long actuators. Colored lines represent mean pressures for each actuator, with shaded areas indicating standard deviations over four cycles.

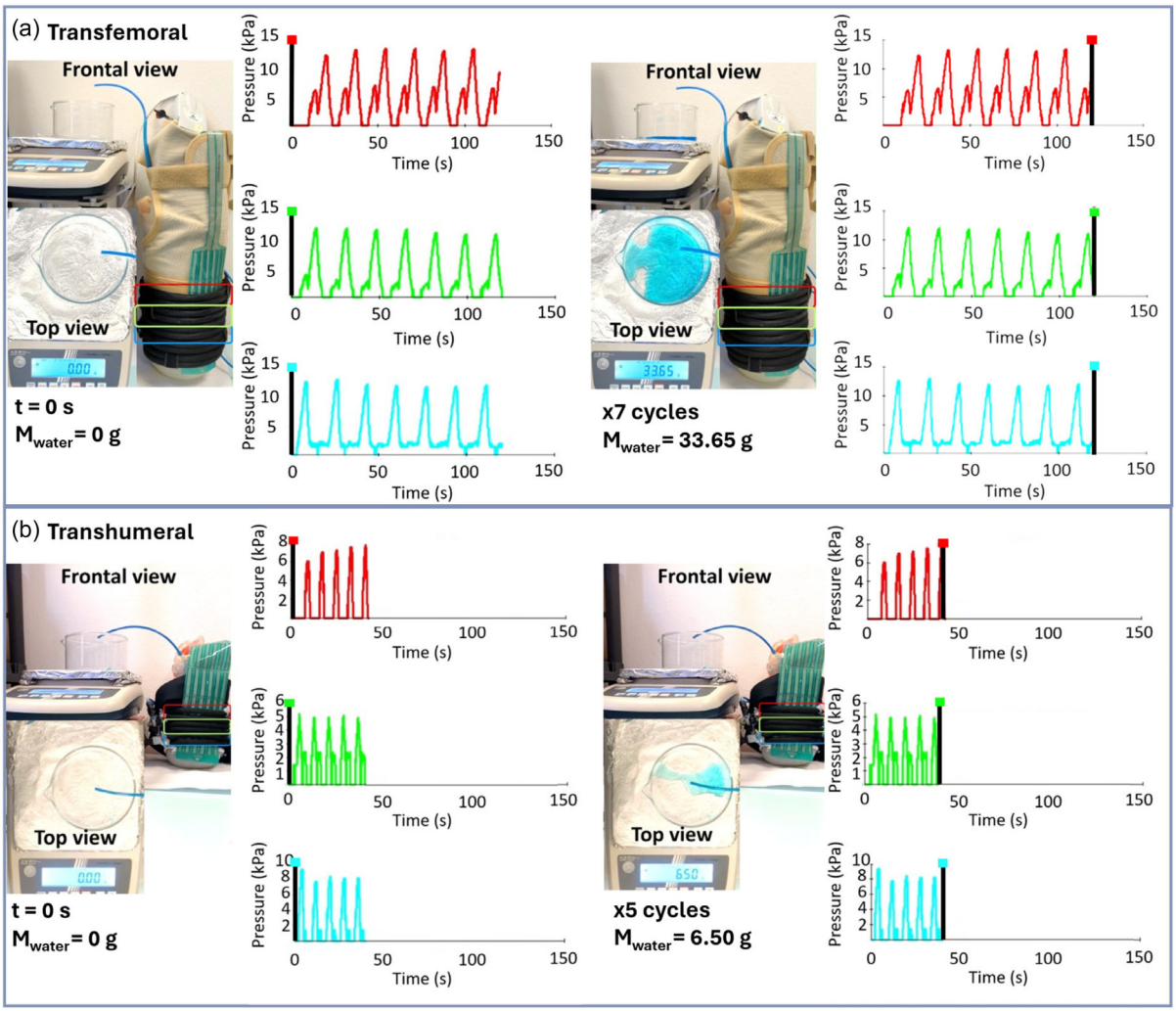

FIGURE 9 | In vitro evaluation of wearable mechanotherapy devices on high-fidelity residual limb simulators representing (a) transfemoral and (b) transhumeral amputations. The simulators' embedded fluidic chambers were filled with colored water to mimic interstitial fluid accumulation. Pressure-time profiles from three distinct actuators (highlighted with red, green, and blue boxes) demonstrate the sequential inflation cycles during therapy. The expelled water is reported before (left) and after (right) actuation, indicating effective fluid displacement: 33.65 mL for transfemoral and 6.50 mL for transhumeral simulators after seven and five actuation cycles, respectively.

3 | Conclusion

In this work, we demonstrate that a wearable soft-robotic system employing McKibben actuators integrated into a textile substrate in a helical configuration can reliably generate the interface pressures required for effective post-operative edema therapy in both upper and lower residual limbs. For the upper-limb system, 50 cm long actuators of 5 and 8 mm diameter were tested as actuation units, while for the lower-limb device, the same diameters were tested in 100 cm length. A wearable or portable control unit manages distal-to-proximal inflation and deflation of the actuators, delivering programmable massage patterns to the residual limb.

During linear characterization, McKibben actuators achieved strains of 26%–28% at 1.5 bar and output forces ranging from 33 to 60 N. When wrapped helically around rigid cylinders, both FEM simulations and bench experiments produced closely aligned interface pressure values: 33.8 and 48.3 kPa (FEM) vs 37.28 ± 0.29 kPa and 45.16 ± 0.35 kPa (experiments) on an 8.5 cm diameter rigid cylinder representing residual arm dimensions, using 5 and 8 mm diameter, 50 cm long actuators, respectively, and 21.2 and 31.9 kPa (FEM) vs 24.40 ± 0.23 kPa and 31.74 ± 0.13 kPa (experiments) on a 15 cm diameter rigid cylinder representing residual leg dimensions, using 5 and 8 mm diameter, 100 cm long actuators, respectively. These values exceeded the 8 kPa upper limit found in clinical compression protocols, confirming the system's capability to span the full therapeutic pressure range. Additionally, on high-fidelity residual limb simulators, the actuators achieved interface pressures of 5–8 kPa (5 mm diameter, 50 cm length) and 9–11 kPa (8 mm diameter, 50 cm length) on the arm simulator, and 6–8 kPa (5 mm diameter, 100 cm length) and 10–13 kPa (8 mm diameter, 100 cm length) on the leg simulator, well within the recommended therapeutic range for post-amputation care and lymphedema management. In vitro tests further demonstrated that sequential distal-to-proximal actuation effectively expelled fluid against gravity from the simulators, replicating the core mechanical action needed for lymphatic drainage. Notably, the system operates at low input pressures (up to 1.5 bar), which enhances both the energy efficiency and safety of the actuation compared to systems relying on alternative actuation technologies (e.g.,

SMAs [15], SMPs [16], or DEAs [17]) or high-pressure pneumatics drives.

Compared with conventional limb compression devices, typically based on bonded or welded pneumatic bladders, our system shows several key advantages in adaptability, dynamic response, and interface pressure control. Existing bladder-based systems commonly employ two to four large chambers per limb, offering poor conformity to complex, curved geometries and resulting in uneven pressure distributions. Additionally, their multilayered construction and larger pneumatic volume result in slower response times and increased bulk, which may compromise wearability and clinical usability. By contrast, our textile-integrated McKibben actuators provide localized, distributed compression and conform naturally to limb contours. Furthermore, the smaller actuator volume and higher mechanical efficiency reduce the required air volume during pressurization, allowing full distal-to-proximal actuation cycles to complete in under 20 s, significantly faster than the 40–60 s cycles typical of commercial devices. This enables more dynamic fluid mobilization and higher treatment frequency.

In comparison to other fluidic soft robotic technologies such as fluidic fabric muscle sheets (FFMSs) [26], our system offers greater control flexibility, more intuitive actuation dynamics, and improved suitability for post-operative edema treatments. In FFMSs, compression is exerted in the unpressurized (resting) state, and pneumatic inflation passively relieves the pressure. In contrast, our system applies compression only when actuated, following a conventional therapeutic logic that mirrors manual lymphatic drainage: compression is introduced via positive inflation and removed by deflation. This allows for fine-grained, programmable control of pressure amplitude, timing, and location.

Future work will focus on the iterative refinement of both the device architecture and its control system. To support configurations requiring a greater number of actuators, and thus faster deflation to maintain the distal-to-proximal sequence within 20 s, the integrated vacuum capability of the micro-compressor will be exploited. In such cases, a dedicated parallel vacuum line could be added to the pneumatic circuit to further reduce deflation time while preserving the intended actuation cycle duration. In addition, integrating flexible pressure sensors into the textile substrate will enable real-time closed-loop control of interface pressure, allowing for further individualized, adaptive therapy. To enhance user comfort and breathability, the device's inner textile layer will be lined with medical-grade polyurethane foam, as recommended by orthopedic specialists. Ultimately, custom-fit devices will be manufactured for amputee participants, and pilot clinical studies will be conducted to rigorously evaluate safety, comfort, and therapeutic efficacy for both upper- and lower-limb applications. These developments aim to bridge the gap between laboratory-stage soft robotics and deployable clinical tools. In the long term, this system has the potential to offer a safe, non-invasive, and home-compatible solution for managing post-amputation edema and supporting functional rehabilitation.

4 | Experimental Section

4.1 | McKibben Actuators

Manufacturing: he mold's 3D geometry for silicone tube manufacturing was designed in SolidWorks (Dassault Systèmes Corp.) and comprised four components: two lateral halves, an upper plate, and a lower plate. Owing to its size, the mold was machined from a Delrin panel and assembled by interlocking the upper and lower plates with the lateral halves. Cylindrical metal rods, matching the desired internal diameter of the silicone chambers, were first inserted into the assembled mold to form the chamber lumens (Supplementary Video 1). The elastomeric tubes were cast from Ecoflex 00-30 silicone (Shore 00-30, Smooth-on, Inc., Macungie, PA, USA). Uncured silicone was prepared by mixing parts A and B in a 1:1 weight ratio and then degassed under vacuum. No mold release was required, as silicone does not adhere to Delrin, facilitating demolding. The silicone mixture was injected into the mold via syringes. After full polymerization, the Delrin mold and metal rods were removed to yield the silicone tubes. Because the mold length was 50 cm, 100 cm actuators were produced modularly: two 50 cm tubes were butt-joined using a small connector rod. The metal rod was extracted by inflating the silicone tube, whose radial expansion allowed the rod to slide out toward one end (see Supplementary Video 1). Each tube was then over braided with a commercial sleeve (Braided sleeving, MULTICOMP PRO). The braided sleeves exhibit a woven structure composed of polymer monofilaments with a nominal diameter of 0.22 mm. Each braid strand is formed by three parallel monofilaments (Table 2). A total of 20 and 24 rhomboidal unit cells is arranged along each circumference of the sleeves with inner diameters of 8 and 10 mm, respectively. Sleeves with inner diameters of 8 mm were used to cover silicone tubes with mean diameters of 5 mm, while sleeves with inner diameters of 10 mm were used to cover silicone tubes with mean diameters of 8 mm. The braided sleeves were stretched and thermoformed using a heat gun to ensure a tight fit around the inner silicone tube, while simultaneously reducing the braid angle and enhancing the actuator's contraction performance. The braided silicone chambers were secured to 3D-printed resin end fittings (one featuring a pneumatic inlet port and one without) using off-the-shelf clamps. End fittings were printed in VeroUltra Black resin on a Stratasys J55 to ensure airtightness. A threaded interface on each fitting allows attachment to a custom mounting bracket, which in turn is clamped to an Instron 5960 (Illinois Tool Works Inc.) for mechanical characterization tests in linear configuration.

4.2 | Wearable Control Unit

Acoustic silencer: the silencer reduces the pump's noise level from 58 dBA to 53 dBA. Measurements were taken using a sound level meter (72 942, Multicomp Pro, USA) in an environment with a background noise level of 42 dBA.

Acknowledgments

The authors sincerely thank the clinical experts Dr. Domenico Alesi and Dr. Amedeo Amoresano for kindly granting us an initial meeting and generously sharing their valuable experience. Their insights were instrumental in better understanding the specific requirements for the device's initial design and development. This work was promoted by INAIL, the Italian National Institute for Insurance against work-related Injuries (noncommercial entity), within the PR23-PAI-P2 eLiner (Cuffia smart con sensoristica integrata e stimoli aptici per il controllo di protesi avanzate) project framework.

Open access publishing facilitated by Scuola Superiore Sant'Anna, as part of the Wiley - CRUI-CARE agreement.

Funding

The authors have nothing to report.

Data Availability Statement

The data that support the findings of this study are available from the corresponding author upon reasonable request.

References

1. J. L. Ng, M. E. Kersh, S. Kilbreath, and M. K. Tate, "Establishing the Basis for Mechanobiology-Based Physical Therapy Protocols to Potentiate Cellular Healing and Tissue Regeneration," *Frontiers in Physiology* 8 (2017): 303, https://doi.org/10.3389/fphys.2017.00303.

2. N. Velazquez and A. Virkus, "Indications for Compression Therapy in Venous and Lymphatic Disease: Consensus Based on Experimental Data and Scientific Evidence," *International Angiology* 27, no. 3 (2008): 193–219.

3. L. Paternò and L. Lorenzon, "Soft Robotics in Wearable and Implantable Medical Applications: Translational Challenges and Future Outlooks," *Frontiers in Robotics and AI* 10 (2023), https://doi.org/10.3389/frobt.2023.1075634.

4. C. Thalman and P. Artemiadis, "A Review of Soft Wearable Robots that Provide Active Assistance: Trends, Common Actuation Methods, Fabrication, and Applications," *Wearable Technologies* 1 (2020): e3, https://doi.org/10.1017/wtc.2020.4.

5. T. Jiralerspong and H. Zhao, "Soft Robotic Devices for Mechanotherapy of the Upper and Lower Extremities," *Advanced Materials Technologies* 10, no. 10 (2025), https://doi.org/10.1002/admt.202401530.

6. B. H. Duhon, T. T. Phan, S. L. Taylor, R. L. Crescenzi, and J. M. Rutkowski, "Current Mechanistic Understandings of Lymphedema and Lipedema: Tales of Fluid, Fat, and Fibrosis," *International Journal of Molecular Sciences* 23 (2022): 12, 6221, https://doi.org/10.3390/ijms23126221.

7. K. Suehiro, N. Morikage, M. Murakami, et al., "A Study of Increase in Leg Volume during Complex Physical Therapy for Leg Lymphedema Using Subcutaneous Tissue Ultrasonography," *Journal of Vascular Surgery: Venous and Lymphatic Disorders* 3, no. 3 (2015): 295–302, https://doi.org/10.1016/j.jvsv.2015.02.001.

8. A. K. Greene, "Epidemiology and Morbidity of Lymphedema," in *Lymphedema: Presentation, Diagnosis, and Treatment* (Springer International Publishing, 2015), 33–44.

9. M. V. Schaverien, J. A. Moeller, and S. D. Cleveland, "Nonoperative Treatment of Lymphedema," *Seminars in Plastic Surgery* 32, no. 1 (2018): 17–21, https://doi.org/10.1055/s-0038-1635119.

10. M. I. Korpan, R. Crevenna, and V. Fialka-Moser, "Lymphedema: A Therapeutic Approach in the Treatment and Rehabilitation of Cancer Patients," *American Journal of Physical Medicine and Rehabilitation* 90, no. 5 (2011): S69–S75, https://doi.org/10.1097/PHM.0b013e31820be160.

11. H. Jamshaid, R. K. Mishra, N. Ahmad, M. Nadeem, M. Muller, and V. Kolar, "Exploration of Effects of Graduated Compression Stocking Structures on Performance Properties Using Principal Component Analysis: A Promising Method for Simultaneous Optimization of Properties," *Polymers* 14, no. 10 (2022): 2045, https://doi.org/10.3390/polym14102045.

12. R. Bjork and S. Ehmann, "STRIDE Professional Guide to Compression Garment Selection for the Lower Extremity," *Journal of Wound Care* 28, no. Sup7 (2019): S1–S44, https://doi.org/10.12968/jowc.2019.28.Sup7.S3.

13. C. S. Lim and A. H. Davies, "Graduated Compression Stockings," *Canadian Medical Association Journal* 186, no. 10 (2014): E391–E398.

14. B. Thompson, K. Gaitatzis, X. Janse de Jonge, R. Blackwell, and L. A. Koelmeyer, "Manual Lymphatic Drainage Treatment for Lymphedema: A Systematic Review of the Literature," *Journal of Cancer Survivorship* 15, no. 2 (2021): 244–258, https://doi.org/10.1007/s11764-020-00928-1.

15. J. H. H. Kim, J. Stilling, M. O'Dell, and C. H. L. Kao, "*KnitDema: Robotic Textile as Personalized Edema Mobilization Device," in Proceedings of the CHI Conference on Human Factors in Computing Systems* (2023), https://doi.org/10.1145/3544548.3581343.

16. B. Kumar, J. Hu, N. Pan, and H. Narayana, "A Smart Orthopedic Compression Device Based on a Polymeric Stress Memory Actuator," *Materials and Design* 97 (2016): 222–229, https://doi.org/10.1016/j.matdes.2016.02.092.

17. T. Kaaya, R. J. Venkatraman, D. Koc, and Z. Chen, "Modeling and Control of Dielectric Elastomer Enabled Cuff Device for Enhancing Blood Flow at Lower Limbs," *IEEE Transactions on Automation Science and Engineering* 21, no. 4 (2024): 6473–6482, https://doi.org/10.1109/TASE.2023.3325617.

18. "*Lympha Press | Compression Pumps & Garments*," accessed August 06, 2025, [Online], https://www.lymphapress.com/.

19. B. Kalita, A. Leonessa, and S. K. Dwivedy, "A Review on the Development of Pneumatic Artificial Muscle Actuators: Force Model and Application," *Actuators* 11, no. 10 (2022): 288, https://doi.org/10.3390/act11100288.

20. M.-S. Kim, J.-K. Heo, H. Rodrigue, et al., "Shape Memory Alloy (SMA) Actuators: The Role of Material, Form, and Scaling Effects," *Advanced Materials* 35, no. 33 (2023), https://doi.org/10.1002/adma.202208517.

21. T. Dayyoub, A. V. Maksimkin, O. V. Filippova, V. V. Tcherdyntsev, and D. V. Telyshev, "Shape Memory Polymers as Smart Materials: A Review," *Polymers* 14, no. 17 (2022): 3511, https://doi.org/10.3390/polym14173511.

22. Y. Guo, L. Liu, Y. Liu, and J. Leng, "Review of Dielectric Elastomer Actuators and Their Applications in Soft Robots," *Advanced Intelligent Systems* 3, no. 10 (2021), https://doi.org/10.1002/aisy.202000282.

23. D. Guan, R. Liu, C. Fei, S. Zhao, and L. Jing, "Fluid-Structure Coupling Model and Experimental Validation of Interaction between Pneumatic Soft Actuator and Lower Limb," *Soft Robotics* 7, no. 5 (2020): 627–638, https://doi.org/10.1089/soro.2019.0035.

24. C. J. Payne, E. G. Hevia, N. Phipps, et al., "Force Control of Textile-Based Soft Wearable Robots for Mechanotherapy," in *IEEE International Conference on Robotics and Automation (ICRA)* (2018): 7062–7069, https://doi.org/10.1109/ICRA.2018.8461059.

25. T. Hakala, A. Puolakka, P. Nousiainen, T. Vuorela, and J. Vanhala, "Application of Air Bladders for Medical Compression Hosieries," *Textile Research Journal* 88, no. 19 (2018): 2169–2181, https://doi.org/10.1177/0040517517716907.

26. M. Zhu, A. Ferstera, S. Dinulescu, et al., "A Peristaltic Soft, Wearable Robot for Compression Therapy and Massage," *IEEE Robotics and Automation Letters* 8, no. 8 (2023): 4665–4672, https://doi.org/10.1109/LRA.2023.3287773.

27. A. J. Comerota, "Intermittent Pneumatic Compression for DVT Prophylaxis," in *Supplement to Endovascular Today* (Academia, 2011), 3–5.

28. "*Buy Fluidic Muscle DMSP Online | Festo GB*," accessed August 6, 2025, [Online], https://www.festo.com/gb/en/p/fluidic-muscle-id_DMSP/.

29. T. Akagi, S. Dohta, H. Kuno, and M. Ihara, "Improvement of McKibben Artificial Muscle with Long Stroke Motion and Its Application," *Journal of System Design and Dynamics* 4, no. 4 (2010): 538–551, https://doi.org/10.1299/jsdd.4.538.

30. R. Morita, H. Nabae, G. Endo, and K. Suzumori, "A Proposal of a New Rotational-Compliant Joint with Oil-Hydraulic McKibben Artificial Muscles," *Advanced Robotics* 32, no. 9 (2018): 511–523, https://doi.org/10.1080/01691864.2018.1464946.

31. N. K. Uppalapati and G. Krishnan, "Towards Pneumatic Spiral Grippers: Modeling and Design Considerations," *Soft Robotics* 5, no. 6 (2018): 695–709, https://doi.org/10.1089/soro.2017.0144.

32. S. Kurumaya, K. Suzumori, H. Nabae, and S. Wakimoto, "Musculoskeletal Lower-Limb Robot Driven by Multifilament Muscles," *ROBOMECH Journal* 3, no. 1 (2016), https://doi.org/10.1186/s40648-016-0061-3.

33. M. Mori, K. Suzumori, M. Takahashi, and T. Hosoya, "Very High Force Hydraulic McKibben Artificial Muscle with a p-Phenylene-2,6-Benzobisoxazole Cord Sleeve," *Advanced Robotics* 24, no. 1-2 (2010): 233–254, https://doi.org/10.1163/016918609X12586209967366.

34. M. Mori, K. Suzumori, S. Seita, M. Takahashi, T. Hosoya, and K. Kusumoto, "Development of Very High Force Hydraulic McKibben Artificial Muscle and Its Application to Shape-adaptable Power Hand," in *Proceedings of the 2009 IEEE International Conference on Robotics and Biomimetics (ROBIO)* (2009), 1457–1462.

35. E. W. Hawkes, C. Majidi, and M. T. Tolley, "Hard Questions for Soft Robotics," *Science Robotics* 6, no. 53 (2021): eabg6049, https://doi.org/10.1126/scirobotics.abg6049.

36. J. E. Sanders and S. Fatone, "Residual Limb Volume Change: Systematic Review of Measurement and Management," *Journal of Rehabilitation Research and Development* 48, no. 8 (2011): 949–986, https://doi.org/10.1682/jrrd.2010.09.0189.

37. R. G. Redhead, "The Early Rehabilitation of Lower Limb Amputees Using a Pneumatic Walking Aid," *Prosthetics and Orthotics International* 7, no. 2 (1983): 88–90.

38. S. Alsancak, S. K. Köse, and H. Altinkaynak, "Effect of Elastic Bandaging and Prosthesis on the Decrease in Stump Volume," *Acta Orthopaedica et Traumatologica Turcica* 45, no. 1 (2011): 14–22, https://doi.org/10.3944/AOTT.2011.2365.

39. National Center for Health Statistics, "*Vital and Health Statistics, Series 3, number 46*," 2015, [Online], https://www.cdc.gov/nchs/products/index.htm.

40. E. Churchill, L. Laubach, J. T. Mcconville, and I. Tebbetts, *Anthropometric Source Book, vol. 1* (NASA Reference Publication, 1978), 1024.

41. C.-P. Chou and B. Hannaford, "Measurement and Modeling of McKibben Pneumatic Artificial Muscles," *IEEE Transactions on Robotics and Automation* 12, no. 1 (1996): 90–102, https://doi.org/10.1109/70.481753.

42. B. Tondu, "Modelling of the McKibben Artificial Muscle: A Review," *Journal of Intelligent Material Systems and Structures* 23, no. 3 (2012): 225–253, https://doi.org/10.1177/1045389X11435435.

43. D. Bruder and R. J. Wood, "The Chain-Link Actuator: Exploiting the Bending Stiffness of McKibben Artificial Muscles to Achieve Larger Contraction Ratios," *IEEE Robotics and Automation Letters* 7, no. 1 (2022): 542–548, https://doi.org/10.1109/LRA.2021.3130627.

44. T. N. Do, H. Phan, T. Q. Nguyen, and Y. Visell, "Miniature Soft Electromagnetic Actuators for Robotic Applications," *Advanced Functional Materials* 28, no. 18 (2018), https://doi.org/10.1002/adfm.201800244.

45. C. Park, C. Ozturk, and E. T. Roche, "Computational Design of a Soft Robotic Myocardium for Biomimetic Motion and Function," *Advanced Functional Materials* 32, no. 40 (2022), https://doi.org/10.1002/adfm.202206734.

46. B. Herren, M. C. Saha, M. C. Altan, and Y. Liu, "Development of Ultrastretchable and Skin Attachable Nanocomposites for Human Motion Monitoring via Embedded 3D Printing," *Composites Part B: Engineering* 200 (2020): 108224, https://doi.org/10.1016/J.COMPOSITESB.2020.108224.

47. M. G. Polizzotto, A. Z. Zaidi, L. Paterno, and A. Menciassi, "*Self-Adaptive Upper Limb Prosthetic Socket," in Proceedings of the IEEE RAS and EMBS International Conference on Biomedical Robotics and Biomechatronics* (IEEE, 2024), 413–418, https://doi.org/10.1109/BioRob60516.2024.10719804.

48. L. Paternò, A. Z. Zaidi, M. G. Polizzotto, et al., "Smart Transfemoral Prosthetic Socket with Motorized Cable-Driven System," *Advanced Intelligent Systems* 7 (2025), https://doi.org/10.1002/aisy.202400995.

Supporting Information

Additional supporting information can be found online in the Supporting Information section.